

UC Berkeley

UC Berkeley Previously Published Works

Title

A Predictive Theory for Domain Walls in Oxide Ferroelectrics Based on Interatomic Interactions and its Implications for Collective Material Properties

Permalink

<https://escholarship.org/uc/item/0qk9r9qx>

Journal

Advanced Materials, 34(7)

ISSN

0935-9648

Authors

Samanta, Atanu
Yadav, Suhas
Gu, Zongquan
et al.

Publication Date

2022-02-01

DOI

10.1002/adma.202106021

Peer reviewed

A Predictive Theory for Domain Walls in Oxide Ferroelectrics Based on Interatomic Interactions and its Implications for Collective Material Properties

Atanu Samanta, Suhas Yadav, Zongquan Gu, Cedric J. G. Meyers, Liyan Wu, Dongfang Chen, Shishir Pandya, Robert A. York, Lane W. Martin, Jonathan E. Spanier, and Ilya Grinberg*

Domain walls separating regions of ferroelectric material with polarization oriented in different directions are crucial for applications of ferroelectrics. Rational design of ferroelectric materials requires the development of a theory describing how compositional and environmental changes affect domain walls. To model domain wall systems, a discrete microscopic Landau–Ginzburg–Devonshire (dmLGD) approach with A- and B-site cation displacements serving as order parameters is developed. Application of dmLGD to the classic BaTiO₃, KNbO₃, and PbTiO₃ ferroelectrics shows that A–B cation repulsion is the key interaction that couples the polarization in neighboring unit cells of the material. dmLGD decomposition of the total energy of the system into the contributions of the individual cations and their interactions enables the prediction of different properties for a wide range of ferroelectric perovskites based on the results obtained for BaTiO₃, KNbO₃, and PbTiO₃ only. It is found that the information necessary to estimate the structure and energy of domain-wall “defects” can be extracted from single-domain 5-atom first-principles calculations, and that “defect-like” domain walls offer a simple model system that sheds light on the relative stabilities of the ferroelectric, antiferroelectric, and paraelectric bulk phases. The dmLGD approach provides a general theoretical framework for understanding and designing ferroelectric perovskite oxides.

ferroelectric oxides for applications in modern nano-electronics such as nonvolatile memories and logic devices for low-voltage operation.^[1,3–7] A high density of domains walls can also endow perovskite oxides with high permittivity and tunability and low loss compared to ordinary dielectric materials.^[8–11] The fascinating properties of ferroelectric perovskites arise from the ability of numerous environmental variables such as composition, strain, pressure, electric field, and temperature to manipulate the polarization of these materials and, in particular, the spatial variations in the polarization that give rise to domains and domain walls that enable a rich variety of response and properties. This ability creates a flexible and responsive platform for materials design. Rational design of DW-related properties in such a large phase space requires a deep understanding of how the changes in the variables (e.g., composition, strain, pressure, electric field, and temperature) affect DW energetics and dynamics.


Despite intense research on ferroelectric perovskites carried out over the last 70 years, the physical understanding of how the behavior of domain walls arises from interatomic interactions is still lacking. Landau–Ginzburg–Devonshire (LGD) theory and density-functional-theory (DFT) calculations have been the main theoretical methods used to describe and understand ferroelectric solid solutions.^[12–15]

1. Introduction

Ferroelectric perovskite oxides are an important class of materials that have been used in a wide range of applications.^[1,2] Domain walls (DW) separating the regions of uniform polarization in a ferroelectric play key roles in the properties of

A. Samanta, S. Yadav, I. Grinberg
Department of Chemistry
Bar-Ilan University
Ramat Gan 5290002, Israel
E-mail: ilya.grinberg@biu.ac.il

Z. Gu, C. J. G. Meyers, L. Wu, D. Chen, J. E. Spanier
Department of Mechanical Engineering and Mechanics
Drexel University
Philadelphia, PA 19104, USA

 The ORCID identification number(s) for the author(s) of this article can be found under <https://doi.org/10.1002/adma.202106021>.

C. J. G. Meyers, R. A. York
Department of Electrical and Computer Engineering
University of California at Santa Barbara
Santa Barbara, CA 93106, USA

S. Pandya, L. W. Martin
Department of Materials Science and Engineering
University of California at Berkeley
Berkeley, CA 94720, USA

L. W. Martin
Materials Sciences Division
Lawrence Berkeley National Laboratory
Berkeley, CA 94720, USA

DOI: 10.1002/adma.202106021

While LGD is a powerful tool for understanding material behavior by compactly describing the system in terms of the order parameter (polarization P for ferroelectric materials), the compactness comes at the price of providing only a phenomenological description of the material that makes LGD fundamentally incapable of predicting changes in the properties due to the changes in composition. Furthermore, to consider the effect of spatial variation in polarization (i.e., the formation of domain structure and domain walls), gradient parameters g_{ij} are used to characterize the energy cost of P variation. These parameters must be derived from scarce experimental data or from first-principles calculations on large cells and are usually assumed to weakly vary with changes in the system such as strain, temperature, and composition. To the best of our knowledge, there is no model of interatomic interactions available for estimating g_{ij} and for evaluating whether or not they can be expected to be constant, for example, with temperature or strain variation. Considering the wide use of LGD theory for modeling of ferroelectrics, this lack of physical understanding of the origin of g_{ij} is an important fundamental problem. In the study of domain-wall kinetics, LGD theory cannot account for the difference in the energies between the A- and B-site centered 180° tetragonal-phase domain walls that give rise to the Peierls potential^[16] (see Supporting Information), since such a difference would require two different values of the g_{44} parameter for the same material which is clearly unphysical. Additionally, LGD calculations cannot be used to estimate barriers for domain nucleation because an arbitrarily small step can be chosen to obtain arbitrarily small nucleation energy.

At the other extreme, DFT calculations can obtain the electronic wave function of the complex system and provide a precise description of the desired properties for essentially any composition and environmental conditions. The complexity of the wave function(s), however, leads to the difficulty in interpreting the DFT results and makes DFT calculations the in silico equivalent of experimental measurements that can accurately evaluate the necessary properties but do not, in and of, themselves provide insight or guidance for materials design. Furthermore, for complex multicomponent solid solutions, the computational cost of DFT evaluation of the many possible domain-wall configurations rapidly becomes prohibitive so that to the best of our knowledge, DFT studies of ferroelectric oxide domain walls have been limited to classic simple materials (e.g., BaTiO_3 , PbTiO_3 , LiNbO_3 , and BiFeO_3 ^[16–27]) with the exception of one study of two ordered $\text{PbZr}_{0.5}\text{Ti}_{0.5}\text{O}_3$ phases.^[28] The effective Hamiltonian method is a DFT-based extension of the LGD approach that can accurately treat the effects of temperature and other perturbations such as strain and electrical boundary conditions.^[29–31] However, a separate first-principles-based derivation for the effective Hamiltonian parameters must be carried out for each composition, making it unsuitable for rapid exploration of compositional-phase space. Therefore, for a fundamental understanding of ferroelectric domain walls and to guide the exploration of the vast possible design space of ferroelectric materials, an analytical predictive theory that describes domain-wall structure and energies in terms of interatomic interactions and relates the properties of the bulk material to the properties of the DW-defect state is necessary.

Here, we use first-principles calculations for ferroelectric bulk unit cells and domain walls to reveal the limitations of the standard LGD approach. We then develop an extension of the LGD theory based on the use of atomic displacements as discrete microscopic order parameters and the interatomic interactions as the terms coupling the order parameters; we call this approach discrete microscopic LGD (dmLGD) theory. Based on the dmLGD approach, we identify A–B repulsion as the interaction that predominantly mediates the coupling of polarization in neighboring unit cells and predicts domain wall energies based on 5-atom, single-domain calculations. Using i) oxygen vacancy pinning of domain walls, ii) thermal fluctuations of the domain walls in the Peierls potential, iii) coercive fields in single-crystal ferroelectric solid solutions, iv) relative stabilities of ferroelectric and antiferroelectric phases and v) relative stabilities of ferroelectric and paraelectric phases as examples, we then demonstrate that the accurate decomposition of the energy of the system into contributions of individual interactions and lattice sites enables predictions of a wide range of properties in different ferroelectrics and the understanding of the effect of compositional variations on material properties based on the results obtained from the simple BaTiO_3 , KNbO_3 , and PbTiO_3 systems only. Our results reveal that there exists a bidirectional relationship between the single-domain material (with uniform polarization) and its DW “defects” (Figure 1). On the one hand, while even the most simple models (i.e., 5-atom unit cell, single domain) contain the necessary information about the interactions to estimate the structure and energy for the DW “defects,” the DW “defects” themselves contain information for predicting the relative stabilities of the ferroelectric, antiferroelectric, and paraelectric single-domain bulk phases. Thus, this work provides an analytical theoretical framework for understanding and designing ferroelectric perovskite oxides.

2. Results

To understand the atomistic origins of the ferroelectric domain-wall energy σ_θ (where θ is the angle between the polarization vectors on the two sides of the domain wall), we study the energies of tetragonal 180° domain walls (σ_{180}) for the classic perovskite ferroelectrics BaTiO_3 (BTO), KNbO_3 (KNO), and PbTiO_3 (PTO) in a variety of strain states (Figure 2). As observed from Figure 2a, for the gradient energy parameter g_{44} that specifies the energy cost of P variation across tetragonal 180° domain wall, standard LGD theory based on P as the order parameter (see S1, Supporting Information) obtains variations of approximately 800%, 600%, and 40% for BTO, KNO, and PTO, respectively, for the strain range of 1.2%. Such a large variation in the gradient energy parameter for a small strain is implausible because a small strain leads to small structural changes and should only weakly affect the interatomic interactions in the material. Thus, the standard LGD approach does not provide a physically meaningful picture for the strain variation effect on domain walls even for these simple systems.

As mentioned above, LGD theory also obtains two different values of the g_{44} parameter for the same material depending on whether the energy of the A- or B-centered domain wall is used for the calculation of g_{44} , which is clearly unphysical

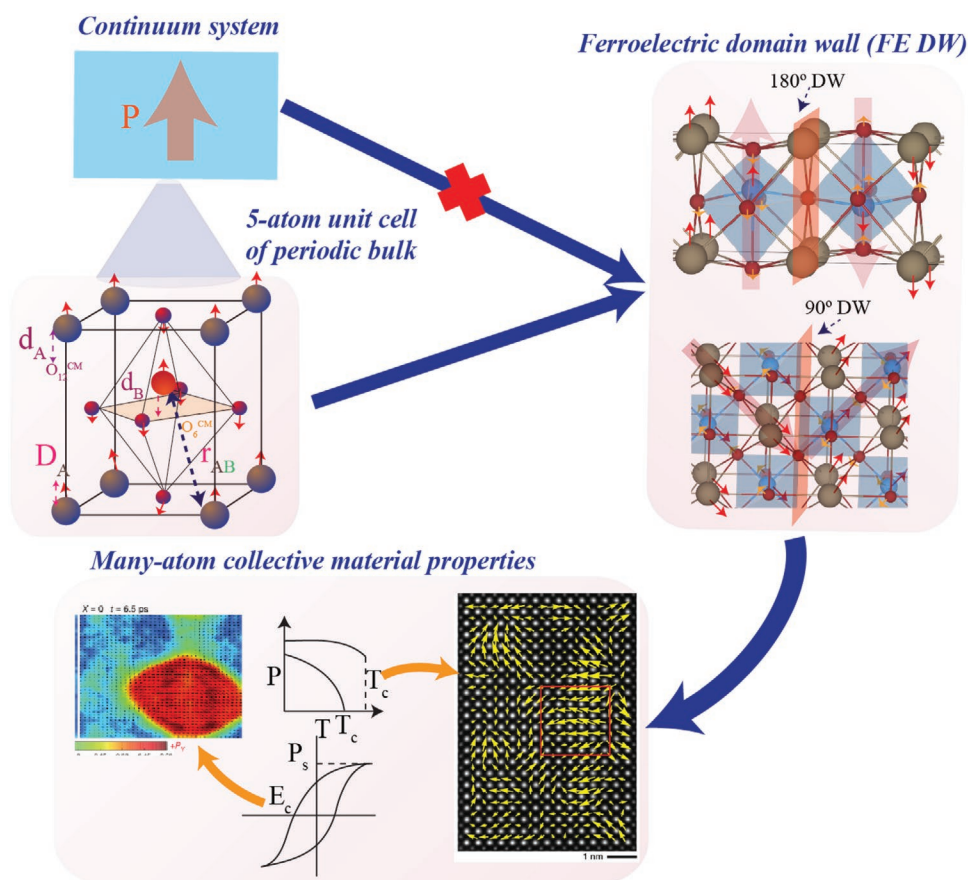


Figure 1. Schematic of the relationship between the simple 5-atom cell, domain walls and collective properties of ferroelectric perovskite oxides. The images in the bottom panel are taken from refs. [40,43]. Left-hand image: Reproduced with permission.^[40] Copyright 2016, Springer Nature. Right-hand image: Reproduced under the terms of the CC-BY Creative Commons Attribution 4.0 International license (<https://creativecommons.org/licenses/by/4.0>).^[43] Copyright 2021, The Authors, published by Springer Nature.

(see S1, Supporting Information). This indicates that it is necessary to go beyond the standard unit-cell-based LGD approach in order to understand the interactions in the material that control σ_ρ .

In the standard LGD approach that describes the bulk system, a macroscopic observable namely polarization is used as an order parameter to accurately describe the free energy surface and the macroscale phenomena and properties of ferroelectrics. Intuitively, to accurately describe microscopic, angstrom- and nanometer-scale potential surface that governs phenomena such as ferroelectric domain walls, the order parameter should be a microscopic variable. While polarization is a measurable bulk property, local polarization is not a rigorously defined observable. By contrast, atomic displacements are well-defined and measurable microscopic variables that are zero for the high-symmetry cubic structure and are non-zero in the ferroelectric state. Therefore, we choose cation displacements at the A-site (d_A) and at the B-site (d_B) as the order parameters for describing the microscopic potential energy surface of ferroelectric perovskites.

We follow the LGD approach of assuming that the potential energy surface of the ferroelectric perovskite can be expressed in a Taylor-series expansion in the powers of d_A and d_B around the high-symmetry structure. Here, a four th-order polynomial

is used to describe the local energy contribution at the A-site and B-site to the total energy.

$$U_{\text{loc}} = U_{\text{loc,B}} + U_{\text{loc,A}} = -0.5a_1d_B^2 + 0.25a_{11}d_B^4 + 0.5b_1d_A^2 \quad (1)$$

Based on previous work,^[32] the coupling between the A- and B-site cation displacements is dominated by short-range cation-cation repulsion between the A- and B-cations. This interaction decays exponentially with the increasing A–B distance, R^{A-B} . Thus, the coupling energy term U_g is given by

$$U_g = \sum_i v_0 \exp(-kR_i^{A-B}) \quad (2)$$

where v_0 and k are constants, the index i runs over the A-site nearest neighbor atoms of site B, and R_i^{A-B} are the distances between the atom on the B-site and its nearest A-site neighbors. In turn, R_i^{A-B} are functions of the off-center displacements of A-site and B-site atoms.

For accurate dmLGD formulation, it is important to distinguish between the different possible definitions of cation displacements. The displacements of the A- and B-site cations can be measured with reference to the center of mass of their O_{12} and O_6 oxygen cages; these displacements change the A–O and B–O bond lengths and bond energies and generate polarization.

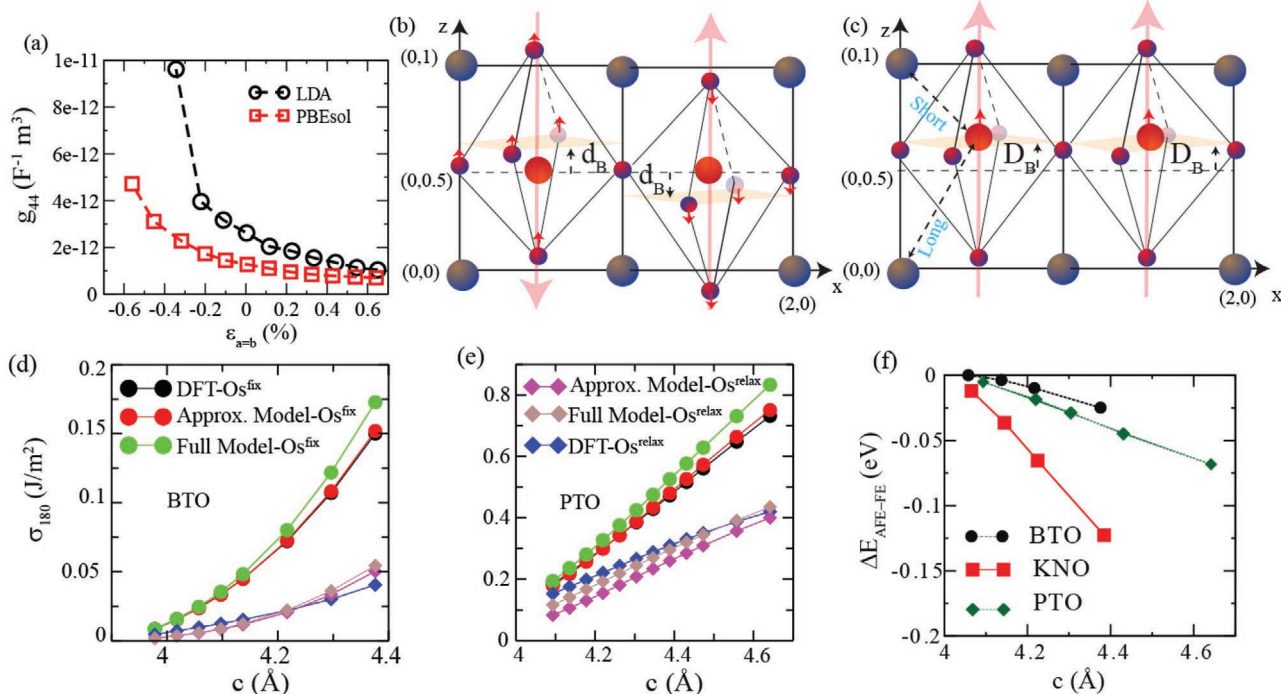


Figure 2. Modeling of 180° domain wall energetics. a) Gradient parameter g_{44} of BTO obtained from DFT calculations as a function of in-plane strain $[\varepsilon_{a=b}(\%) = (a - a_{eq})/a_{eq}]$ using standard LGD theory. b,c) 2D schematic representation of FE ABO_3 perovskite. The direction of atomic displacement and unit cell is shown by red color arrows and a rectangular box. A, B, and O atoms are shown by black, orange, and red spheres. The short- and long-range distance between the A–B atoms is shown by black dotted line. b) Tilting of O_6 oxygen cages without changing the A–B cation distance and displacement d_B of the B-cation atom with reference to the center of mass of their O_6 oxygen cages. c) Shows B-cation displacements D_B with reference to the B-site positions in the high-symmetry structure. Similarly, we can define for A-cations, d_A with reference to the center of mass of their O_{12} oxygen cages and D_A with reference to the A-site positions in the high-symmetry structure. d,e) Show the 180° DW energy as function of c lattice parameter and share legends. f) Energy difference between the antiferroelectric and ferroelectric state as a function of c lattice parameter. Here, the antiferroelectric and ferroelectric states are considered by keeping O and A-site ions fixed at their symmetric positions).

We denote these displacements by d_A and d_B , respectively. Since d_B is defined with respect to the center of the O_6 cages, a shear of the O_6 octahedra even without any shift of the A- and B-cations from the high-symmetry positions will generate non-zero d_B and local dipole moments while preserving the symmetric distances between the A- and B-cations (Figure 2b). Alternatively, it is possible to define the A- and B-cation displacements with reference to the A- and B-site positions in the high-symmetry structure. We denote these displacements as D_A and D_B . These displacements may not change the A–O and B–O distances in the case where the oxygen cages displace together with the cations, but will change the A–B distances and the A–B repulsive interactions if D_A and D_B are different (Figure 2c). Thus, d_A and d_B should be used to describe the energetics of the A–O and B–O interactions, and D_A and D_B should be used to describe the energetics of the A–B interactions. While the question of which definition of ionic displacement should be used may appear to be highly technical, as we will see it plays a key role in modeling domain energies because it is intimately related to the chemical bonding and interatomic interactions in the material.

For a perovskite with A- and B-cation displacements D_A and D_B from the high-symmetry A- and B-site positions, the coupling energy term due to A–B cation repulsion can be rewritten as

$$U_g = g(D_A - D_B)^2 \quad (3)$$

by using the Taylor expansion of the exponential repulsive interaction between the A- and B-site cations (see S2–S4, Supporting Information). The g constant here will not have the same values as the g_{ij} in the LGD theory. However, it can be shown that dmLGD becomes equivalent to LGD theory in the limit of slow spatial variation of polarization and ionic displacements (see Supporting Information). The total energy of the bulk ferroelectric system with respect to the high-symmetry structure is described by

$$U_{\text{tot}} = -0.5a_1d_B^2 + 0.25a_{11}d_B^4 + 0.5b_1d_A^2 + g(D_A - D_B)^2 \quad (4)$$

and for a system with spatially varying ionic displacements, the total energy is given by

$$U_{\text{tot}} = \sum_i [-0.5a_1d_B^2 + 0.25a_{11}d_B^4 + 0.5b_1d_A^2 + g(D_A - D_B)^2] \quad (5)$$

where the index i runs over the unit cells of the perovskite in the material and U_{tot} is the total energy difference between the ferroelectric and paraelectric states. Since the driving force for ferroelectric distortion is controlled by changes in the bond lengths in the local A– O_{12} and B– O_6 environments,^[32] the local

Table 1. Calculated a_1 , a_{11} , b_1 , and g parameters obtained using the PBEsol functional.

System	$a = b$ [Å]	c [Å]	a_1 [Ry Å ⁻²]	a_{11} [Ry Å ⁻⁴]	b_1 [Ry Å ⁻²]	g [Ry Å ⁻²]
BTO	3.9705	4.0178	0.3622	14.2926	0.1973	0.1326
KNO	3.9688	4.0652	0.6268	21.0312	0.0943	0.0828
PTO	3.8834	4.1354	0.5006	9.1878	-0.1328	0.1314

energy due to the distortion that is represented by the first two terms is controlled by d_A and d_B , and is parameterized by the material- and strain-state-specific constants a_1 , a_{11} , and b_1 . For a bulk system, the parameters a_1 , a_{11} , and b_1 can be obtained from fitting the energies of a series of DFT calculations for bulk 5-atom structures with different values of A- and B-cation displacements to Equation 4 as described in Tables S1–S6 (Supporting Information). The calculated a_1 , a_{11} , b_1 , and g values of BTO, KNO, and PTO at selected lattice parameters are reported in Table 1 (see Supporting Information for a_1 , a_{11} , b_1 , and g values for additional lattice parameter values, Tables S1–S6, Supporting Information).

For bulk systems, dmLGD is equivalent to the standard LGD theory and can be used to make the same predictions regarding the properties of the ferroelectric system at different temperatures, pressure, and applied electric field conditions. Going beyond the capabilities of the standard LGD approach, Equation (5) can be used to accurately the energies of systems with spatially varying polarization such as the domain wall energies σ_θ for different θ . This is because the first two terms of Equation (5) give the local energy U_{loc} while the last term represents the gradient-energy term U_g because it disfavors variations in the ionic displacements in different unit cells of the material (see Supporting Information). In contrast to the standard LGD approach where a single-domain configuration does not contain any information regarding U_g , the more detailed atomistic approach contains information about the energy cost of the polarization gradient U_g even at the level of a 5-atom unit cell, single-domain state and therefore can be used to predict the energies of different domain walls. This is a crucial advantage of the discrete microscopic approach.

Furthermore, the discrete nature of the order parameter more accurately describes the potential energy surface that is due to the interactions between discrete atoms. This is illustrated in Figure S6 (Supporting Information) showing the domain wall profiles in the continuous P and discrete d_B and d_A representations for a system with the preference for off-center displacement at the B-site and the preference to remain at the high-symmetry position for the A-site (e.g., BaTiO₃). While the local energy cost of the continuous P representation is large due to the zeroing out of P at the A-site centered domain wall, the local energy cost in dmLGD is low due to the preference of the A-site to remain at the high-symmetry position. Since the true order parameters in ferroelectrics, namely ionic displacements, are in fact discrete and are only approximated in a coarse-grained model by the continuous P order parameter, the minimum grid size for LGD simulations of ferroelectric perovskites must either one half or one lattice constant, leading to a finite energy of nucleation processes.

Formally, the dmLGD theory expressed by Equation (4) describes the potential energy surface of a 1D ferroelectric (e.g., tetragonal BTO or PTO). In a manner similar to that for the standard LGD theory, the dmLGD expression given in Equation (4) can be extended to three dimensions and to include strain effects by using the x -, y -, and z -components of ionic displacements and the strain as the order parameters. Similarly, coupling to additional order parameters such as octahedral tilting and magnetization can also be included in a manner similar to that of the standard LGD theory.^[29–31] The dmLGD approach can also be extended to describe the effects of compositional changes (A- and B-site substitution and introduction of O vacancies) through the appropriate changes in the a_1 , a_{11} , and b_1 parameters as revealed by DFT calculations. The effects of temperature and pressure can also be included by assuming linear dependence of the a_1 and b_1 parameters on temperature and pressure.

More importantly, as will be illustrated below, even without a formal extension of dmLGD to the description of compositional and environmental variations, the discrete and physically meaningful description of the potential energy surface of the ferroelectric by the dmLGD approach enables predictions of the effects of the changes in composition (e.g., from BaTiO₃ to PbTiO₃ or due to the introduction of O vacancies) on different ferroelectric properties and the relative stabilities of the different phases of the material (e.g., ferroelectric, antiferroelectric, and paraelectric) based on simple structural and energetic criteria.

We now apply the dmLGD approach to the modeling of ferroelectric domain walls. We first calculated 180° domain wall energy (σ_{180}) only allowing the cations to displace while freezing the oxygen ions at their high-symmetry positions (O-fixed) and analyzed the energetics of the system in terms of A- and B-site displacements using Equation (5). We fit a_1 , a_{11} , b_1 , and g to the results of DFT calculations on 5-atom unit cells with different A- and B-site cations (see S3, Supporting Information) and using the fit values to predict the energies for the oxygen-fixed 180° DWs. Even though for all of our 5-atom calculations, the system has uniform polarization, we obtained good agreement with the DFT oxygen-fixed σ_{180} values for the domain-wall configuration with non-uniform polarization (Figure 2d,e).

Consideration of the dipole–dipole interactions at the 180° domain wall shows that an attractive interaction will be present between the dipoles formed by the titanium (100) displacements on the two opposite sides of the domain wall. This interaction decreases σ_{180} and likely accounts for the overestimation of σ_{180} by our model. The presence of this dipole–dipole interaction also means that in the absence of A-site (B-site) displacement that couples to the B-site (A-site) displacements in the neighboring cells, the anti-parallel displacement pattern will be preferred. This is demonstrated by the plot of the DFT-calculated energy difference between the antiferroelectric and ferroelectric states with the A-site atoms fixed at high-symmetry positions that shows that the antiferroelectric state is preferred, with the preference increasing with greater c lattice parameter and B-cation displacement (Figure 2f and see S6, Supporting Information). Thus, our results show that it is the A–B repulsion that is responsible for the gradient-energy cost of polarization variation and the appearance of the ferroelectric

phase while in the absence of the ability to minimize this repulsion by coupled A- and B-displacement, the usual preference of dipolar systems for antiparallel (antiferroelectric-like) arrangement will be restored.

Comparison of the oxygen-fixed σ_{180} and fully relaxed σ_{180} values show that oxygen relaxation is quite important for domain-wall energies, with much higher domain-wall energies (by a factor of 1.5–4) obtained for the oxygen-fixed case. Examination of the relaxed DFT domain-wall structure (Figure 2b) shows that the O_6 octahedra at the domain wall shear, substantially decreasing the displacement of the titanium cations at the domain wall relative to the A-site cation. We note that the local energy of the B-site displacement is controlled by d_{Ti} that can be created by the O_6 -shear mode. By contrast, the gradient-energy term in Equation 5 is controlled by D_{Ti} and is not affected by the O_6 -shear mode. Thus, the activation of the O_6 shear simultaneously keeps the local energy U_{loc} low because d_{Ti} is approximately equal to the single-domain d_{Ti} and keeps the gradient U_g low due to the small D_{Ti} and small change in the A–B cation distance. The energy cost of O_6 shear is low and thus, avoidance of the trade-off between U_g and U_{loc} dramatically lowers the domain-wall energy relative to oxygen-fixed domain wall energies.

Assuming that the energy cost of the shear mode is zero and that D_{Ti} is equal to one half of the single-domain value D_A value (see S5, Supporting Information), we evaluated σ based on the a_1 , a_{11} , b_1 , and g constants obtained from 5-atom calculations to obtain the lower-bound estimate of σ_{180} . Good agreement (Figure 2d,e) is obtained between the model and DFT values

with the underestimation accounted for by our neglect of the O_6 -shear-mode cost (which increases with higher strain).

Having elucidated the energetics of σ_{180} in terms of A- and B-site displacements, we consider the tetragonal 90° and rhombohedral 71° domain walls (Figure 3 and Figure S7, Supporting Information) that control the switching and E_c in bulk ferroelectrics.^[33] Figure 3a,e shows the domain wall structure and Figure 3b,d shows the polarization profiles of these domain walls. In contrast to the 180° domain walls, these domain walls exhibit dipole–dipole interactions that are less favorable for the domain wall than for the single domain, giving rise to a contribution to σ_{90} and σ_{71} that is proportional to P^2 . Interestingly, we find that the A–B cation repulsion energy for the stable oxygen-centered 90° domain wall is slightly lower than that in the single-domain structure (Figure 3c, and S7, Supporting Information). By contrast, the A–B centered 90° domain wall exhibits a very high A–B cation repulsion energy and is unstable. Thus, we conclude that σ_{90} is essentially due to dipole–dipole interactions and scales approximately as P^2 . For the 71° rhombohedral-phase domain wall, the domain-wall energy σ_{71} is also dominated by the dipole–dipole interactions proportional to P^2 and the A–B cation repulsion contribution is slightly positive (Figure 3f, and S7, Supporting Information).

We also consider the application of the dmLGD approach to 71° and 180° conducting domain walls ($71^\circ c$ and $180^\circ c$) formed by tail-to-tail and head-to-head arrangements of local dipoles. The polarization profiles for these domain walls are generated following the approach of Petralanda et al.^[34] and are shown in Figure 4a,b. For these domain walls (centered on the A-site),

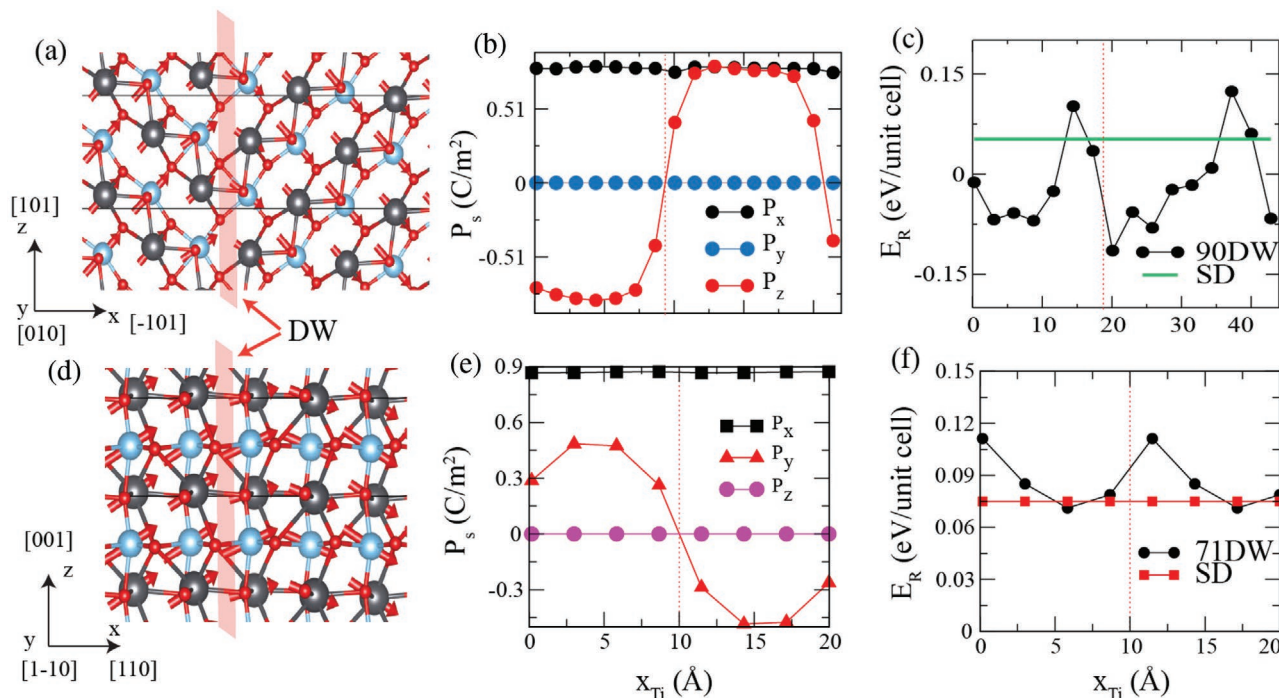


Figure 3. Modeling of 90° and 71° domain walls. a) 90° tetragonal FE DW structure of PTO. b,c) Polarization and A–B repulsive energy per unit cell of 90° DW as a function of Ti x-coordinate of PTO relaxed structure. d) 71° rhombohedral FE DW structure of PTO. e,f) Polarization and A–B repulsive energy per unit cell of 71° DW as a function of Ti x-coordinate of PTO relaxed structure. 71° DW of PTO is constructed with the lattice parameter of 4.0 Å and the unit cell is similar to the 71° DW BaTiO₃ published by Taherinejad et al.^[24] The black, cyan, red spheres represent Pb, Ti, and O atoms. Local polarization direction is shown by the red arrows.

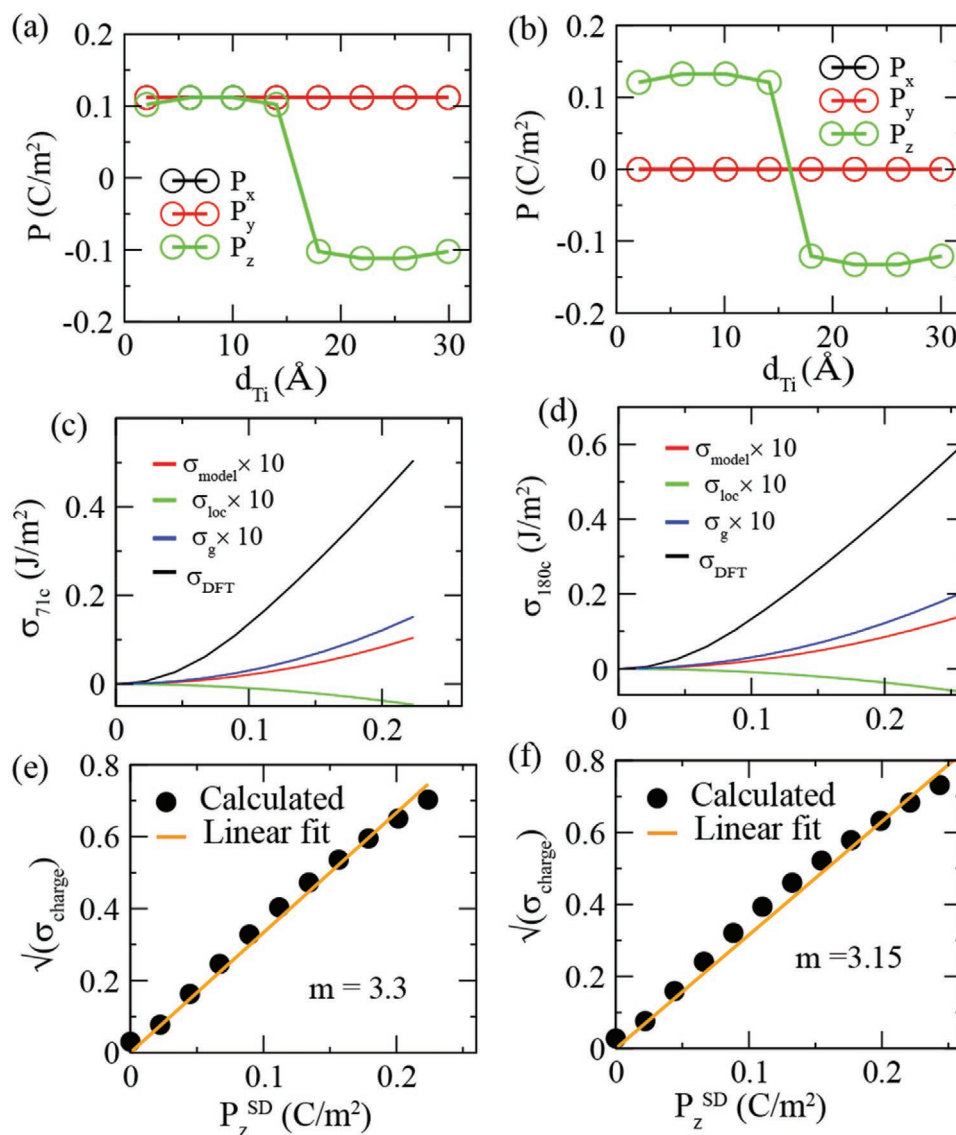


Figure 4. Modeling of charged 71° and 180° domain walls. a,b) The polarization components as a function of Ti position for 71° and 180° BTO charged domain walls. c,d) Calculated domain wall energy using DFT and the dmLGD model as a function of the z-component of single-domain polarization. σ_{model} , σ_{loc} , and σ_{g} are total energy, local energy, and gradient energy calculated by the dmLGD model equation. σ_{model} , σ_{loc} , and σ_{g} values are multiplied by 10 for clear visualization. The $1 \times 1 \times 8$ supercell of the rhombohedral and tetragonal unit cell is considered for the 71° and 180° BTO charged domain wall. The lattice parameters of the rhombohedral and tetragonal unit cell are $a = b = c = 4.0 \text{ \AA}$ and $a = b = 3.97 \text{ \AA}$, $c = 4.0177 \text{ \AA}$. The charged domain wall energy is calculated by keeping the oxygen atoms fixed to their symmetric position for this study (for details, see Supporting Information). e,f) Square root of the difference between the domain wall energies obtained by DFT and the dmLGD model ($\sqrt{\sigma_{\text{charge}}}$) as function of the z-component of single-domain polarization (P_z^{SD}). The linear equation $y = mx$ is used to fit the $\sqrt{\sigma_{\text{charge}}}$ vs P_z^{SD} plot, as shown by the orange solid lines.

the domain wall energy σ will have local energy and repulsive energy contributions as well as a contribution due to the creation of the bound charge at the domain wall as expressed by

$$U_{\text{tot}} = U_{\text{loc}} + U_{\text{g}} + U_{\text{charge}} \quad (6)$$

$$U_{\text{charge}} = C_0 (\Delta P)^2 \times A \quad (7)$$

where ΔP is the change in the polarization across the domain wall and C_0 and A are constant and area perpendicular to the polarization variation. For different values of the polarization

inside the domain, we evaluate the DFT domain wall energies for these domain walls as well as our model local energy and repulsive energy contributions using the a_1 , a_{11} , b_1 , and g parameters obtained from 5-atom bulk DFT calculations, with the results shown in Figure 4b,c. We then take the difference between the DFT-calculated σ values and the $U_{\text{loc}} + U_{\text{g}}$ contributions to the domain wall energy to obtain the U_{charge} contribution to the domain wall energy (σ_{charge}) for different values of P inside the domain (Figure 4b,c). Plotting the $\sqrt{\sigma_{\text{charge}}}$ versus P inside the domain (Figure 4d,e), we find that for both 71°c and 180°c walls and for the BTO, KNO and PTO materials,

U_{charge} exhibits a universal dependence on the bound charge $(\Delta P)^2$ at the domain wall with the value of C_0 varying between 2.4 and $3.3 \text{ J m}^2 \text{ C}^{-2}$. Here, $C_0 = \left(\frac{m}{2}\right)^2$, where m is the slope of

the linear fit of $\sqrt{\sigma_{\text{charge}}}$ vs P . Thus, our dmLGD approach is also suitable for the modeling of conducting domain walls.^[35]

The physical understanding of the domain wall energetics in terms of discrete ionic displacements and the interatomic interactions enabled by dmLGD theory makes it a general and broadly useful tool for modeling of ferroelectrics domain walls that can be used to predict various domain-wall related properties of a wide range of ferroelectric perovskite materials based on the findings for the simple BTO, KNO, and PTO systems only. We illustrate this by using the physical understanding obtained by our dmLGD theory for BTO, KNO, and PTO to predict the effects of compositional variations on: i) oxygen vacancy migration energies, ii) Peierls potential and thermal fluctuations of domain walls, iii) coercive fields in ferroelectric solid-solution crystals, iv) relative stabilities of ferroelectric and antiferroelectric phases and v) ferroelectric-to-paraelectric transition temperatures.

Oxygen vacancies have been considered to be a primary cause of domain wall pinning that hinders switching in ferroelectrics and the preference for the vacancy to be located at the 180° domain wall rather than inside the domain was confirmed for PbTiO_3 by DFT calculations^[36] but was not studied for other materials. Our dmLGD analysis of the potential energy surface for BTO, KNO, and PTO shows that the b_1 parameter is negative for PTO while it is positive for KNO and BTO, indicating that Ba and K prefer to remain in the high-symmetry position while Pb prefers to displace from the high-symmetry position. This means that the Pb–O bonds for the Pb at the 180° Pb-centered domain walls are weaker than the Pb–O bond of Pb atoms in the bulk of the domain, whereas the Ba–O and K–O bonds at the domain wall are stronger than the Ba–O and K–O bonds of the Ba and K atoms inside the domain. Since the introduction of the O vacancy into the material incurs the cost of A–O bond breaking, the introduction of the vacancy at the 180° domain wall is favorable in PTO (because weaker bonds are being broken), while for BTO and KNO the vacancy formation energy should be higher at the domain wall. To confirm this prediction, we carried out DFT calculations for BaTiO_3 and PbTiO_3 supercells containing a 180° domain wall and an oxygen vacancy at different positions. As shown in Figure 5, in agreement with our expectations, a strong preference of the vacancy to be located at the 180° domain wall is observed for PbTiO_3 as indicated by the lower vacancy formation energy, while for BaTiO_3 the vacancy formation energy is lowest inside the domain. This suggests that domain wall pinning by vacancies will be either weak or entirely absent in BaTiO_3 and KNO_3 .

Next, we consider the effect of compositional change in the $\text{Ba}_{1-x}\text{Sr}_x\text{TiO}_3$ (BST) solid solution on the Peierls potential and thermal oscillations of 180° domain walls. Domain wall motion can be considered to proceed on a Peierls potential formed by the difference between the energies of the A-site and B-site centered domain walls.^[37] In particular, domain wall motion can take the form of the random oscillations of the domain wall due to thermal fluctuations. The thermally driven hopping of the 90° domain walls in orthorhombic-phase BST thin films

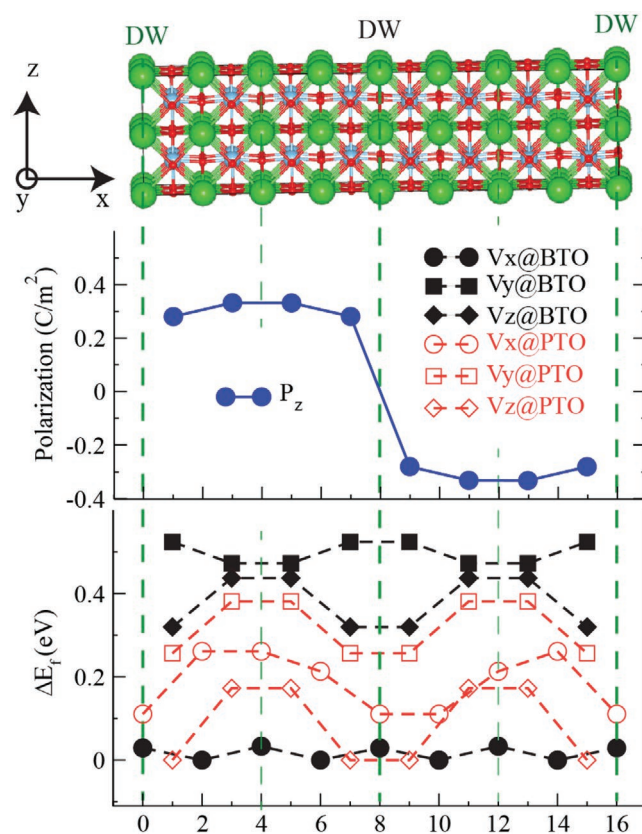


Figure 5. Potential for oxygen vacancy migration in BaTiO_3 and PbTiO_3 . Oxygen vacancy formation energy at different locations in the 180° DW structure of PTO and BTO tetragonal perovskites. $8 \times 2 \times 2$ supercell is considered for calculating the oxygen vacancy formation energy using the SIESTA code (for details, see Supporting Information). The green, cyan, and red spheres represent Ba, Ti, and O atoms. The green solid dotted lines show the BaO plane. The z-component of the polarization as a function of TiO_2 plane position for BTO 180° DW is shown by solid blue-filled circles. The vacancy formation energy is calculated as $E_f^0 = (E_{\text{total}}^0 + 0.5E_{\text{O}_2}) - E_{\text{bulk}}$ where E_{total}^0 and E_{bulk} are the total energies of the system containing an oxygen vacancy and without oxygen vacancy, respectively. E_{O_2} is the total energy of an oxygen molecule in the gas phase. $\Delta E_f = E_f^0 - E_{f,\text{min}}^0$ and $E_{f,\text{min}}^0$ is the lowest oxygen formation energy.

(aa_1/aa_2 domain variant) with T_c close to room temperature has been shown to give rise to resonance effects and spikes in the quality factor (Q) spectrum under an application of an in-plane external bias field.^[8] However, such spikes are absent in the absence of the external bias field due to a too-high barrier for thermal domain wall oscillations. By contrast, a system with a low barrier for thermal domain wall oscillations, i.e., a flat Peierls potential can be expected to display thermal domain wall oscillations even in the absence of an external bias field. Here, we use the dmLGD approach to predict that increasing BST content will lead to a rapid flattening of the Peierls potential in tetragonal BST films.

For thin films of tetragonal ferroelectrics, the switching of the out-of-plane polarization is controlled by the movement of 180° domain walls.^[33] In BTO, since the energy cost of the Ba-centered 180° domain wall (σ_{Ba}) is due to the increased Ba–Ti repulsion at the DW, it depends on the difference between the barium and titanium displacements $D_{\text{Ba}} - D_{\text{Ti}}$. On

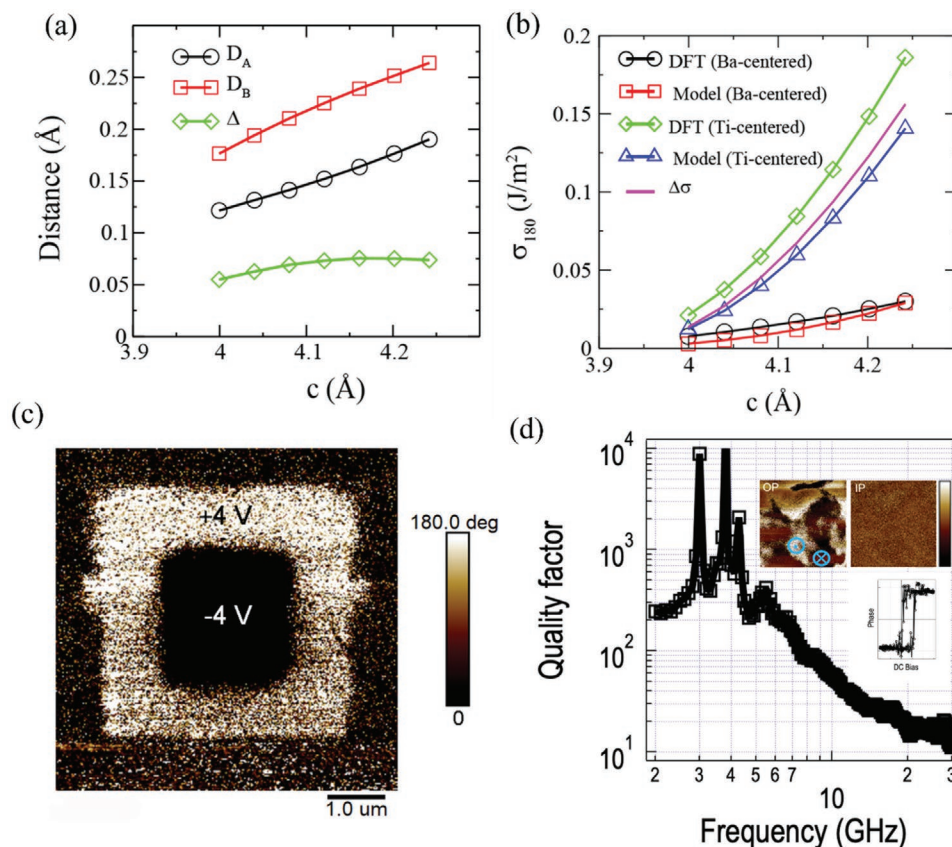


Figure 6. Prediction of material properties based on an analytical model. a) D_A , D_B , and $\Delta = (D_B - D_A)$ as function of c . D_A and D_B show linear variation with c , and Δ versus c shows that it is more or less constant. Ba-centered domain wall energy is mainly due to the repulsion energy contributed (as shown in Figure S18, Supporting Information). The repulsive energy contribution to the σ_{180}^{Ba} is given by (for details see Equation S19, Supporting Information) $\sigma_{180} = g(0 - D_B^{\text{DW}})^2 + g(D_A^{\text{SD}} - D_B^{\text{DW}})^2 - 0.5b_1(d_A^{\text{SD}})^2 - 2g(D_A^{\text{SD}} - D_B^{\text{SD}})^2$. Therefore, slow variation of Δ implies that σ_{180}^{Ba} will go down slowly with the c parameter. b) σ_{180}^{Ti} and σ_{180}^{Ba} as function of c lattice parameter of BTO (DFT and model calculations are considered using LDA functional and Equation (1)). $\Delta\sigma = \sigma_{\text{Ti-centered}} - \sigma_{\text{Ba-centered}}$ is the difference between the Ti-center and Ba-center DW energies of BTO 180° DW that give the height of the Peierls potential. c) Piezoresponse force microscopy map of a written box-in-box pattern. d) Room-temperature microwave frequency-dependent quality (Q) factor as a function of frequency for c^+/c^- $\text{Ba}_{0.7}\text{Sr}_{0.3}\text{TiO}_3$ film (experimental). Resonances are explained by thermal fluctuations of 180° DWs. Q factor of a 100 nm-thick epitaxial $\text{Ba}_{0.7}\text{Sr}_{0.3}\text{TiO}_3/\text{GdScO}_3(110)$ interdigitated electrode capacitor, exhibiting zero bias external electric field resonance spikes between 2 and 5 GHz well above the background. The insets show representative out-of-plane (OP) and in-plane (IP) piezoresponse force microscopy (PFM) images for the BST film confirming the presence of the c^+/c^- DW variant with directions denoted in blue, and the piezoresponse voltage-phase hysteresis further confirming local ferroelectricity in the film. The area of the PFM image is $500 \times 500 \text{ nm}^2$ and the color-map corresponds to negative and positive system phase.

the other hand, the energy of the Ti-centered 180° domain wall (σ_{Ti}) is due to the energy cost of zeroing out the titanium displacement and depends on d_{Ti} . As seen from Figure 6a, $D_{\text{Ba}} - D_{\text{Ti}}$ changes more weakly with the changes in the c parameter (and P) than d_{Ti} , suggesting weaker dependence of σ_{Ba} on P compared to σ_{Ti} . In fact, for BTO, both our model and DFT calculations predict that σ_{Ba} scales as $P^{1.9}$ while σ_{Ti} scales as P^3 (Figure 6b and S11, Supporting Information).

This difference in the P scaling between σ_{Ba} and σ_{Ti} implies that the application of tensile strain decreases the c/a lattice parameter ratio and P will strongly decrease σ_{Ti} but will more weakly decrease σ_{Ba} . Thus, for a sufficiently small P (due to a small c lattice parameter, see S11, Supporting Information), the Peierls potential given by $\sigma_{\text{Ti}} - \sigma_{\text{Ba}}$ will become flat or close to flat (Figure 6), enabling rapid thermal oscillations of domain walls. Since our analytical model and DFT results show that D_A and D_B are controlled by the c lattice parameter (see S11, Supporting Information), the flattening of the Peierls poten-

tial and thermal domain-wall fluctuations should also occur when the c , P , and U_{loc} of BTO are decreased by mixing with SrTiO_3 to obtain $\text{Ba}_{1-x}\text{Sr}_x\text{TiO}_3$ (BST) solid solutions. Based on our previous results,^[37] the presence of thermal hopping of 180° domain-walls should lead to the appearance of resonance peaks in the Q spectrum of tetragonal c^+/c^- BST films with higher SrTiO_3 content and a high density of 180° domain walls even in the absence of the external electric field.

To confirm our predictions, we grew $x = 0.3$ BST films on $\text{GdScO}_3(111)$ substrate because according to the BST phase diagram for this strain and composition the BST film will be found in the tetragonal phase with T_c close to room temperature (see S15–S18, Supporting Information) and examined their Q spectrum. Examination of reciprocal space maps showed that the films are tetragonal and piezoresponse force microscopy (PFM) experiments revealed polarization profiles consistent with the c^+/c^- domain configuration with a high density of 180° domain walls (Figure 6c). As shown in Figure 6d, the

Q spectrum measurements performed for these BST films without an application of a bias showed high resonance peaks between 2 and 5 GHz. The presence of these resonance peaks indicates the existence of strong thermally driven hopping of 180° domain walls, consistent with the flattening of the Peierls potential predicted by our dmLGD calculations.

For our third example of the application of physical understanding extracted from the dmLGD model, we consider the prediction of the compositional variation of the coercive field E_c for bulk rhombohedral ferroelectric perovskite oxides. In this case, the switching of polarization proceeds through the motion of 71° domain walls and the energy required for ferroelectric switching is characterized by the coercive field E_c that is a crucial material parameter for many applications. For these materials, the coercive field E_c at the temperature T [$E_c(T)$] scales with $\sigma_{71}(T)^2/P(T)$ [$\sigma_{90}(T)^2/P(T)$]^[33] and since σ_{71} (σ_{90}) is largely due to dipole–dipole interactions and scales with P^2 , we obtain $E_c(T) \sim P^3(T)$. According to simple Landau theory $P(T) = (P_0^2/T_c)(T - T_c)^{1/2}$, where P_0 is the 0 K polarization. Since our analysis of domain-wall energies showed that σ_{71} is dominated by the P^2 contribution and T_c is empirically known to scale as P_0^2 ,^[38–42] we obtain $E_c(300\text{ K}) \sim (T_c - 300)^{1.5}$. To test this prediction, we collected the experimental results for room temperature E_c and T_c from the literature (References for experimental T_c and E_c data are given in Section S14, Supporting Information) for 14 different single-crystal ferroelectric perovskite oxide solid solution compositions (see Section S13, Supporting Information) and then plot the room temperature E_c values versus the corresponding T_c values (Figure 7a). It is found that the experimental E_c and T_c data show good agreement with the predicted $E_c(300\text{ K}) \sim (T_c - 300)^{1.5}$ relationship. We note that this relationship allows an easy evaluation of the intrinsic E_c of a material that is difficult to obtain either by direct measurements (due to the presence of imperfections such as grain boundaries, vacancies, and impurities) or by P measurements due to the effects of the electrode-oxide interface on the measured P values. By

contrast, T_c values are easy to measure and are only weakly affected by the imperfections in the material.

We now discuss how the relative stabilities of the different phases of bulk single-domain materials (e.g., ferroelectric, antiferroelectric, and paraelectric) can be predicted from the simple structural criteria based on the information provided by the study of the DW “defects” with the dmLGD approach. We first focus on the relative stability of the ferroelectric and antiferroelectric phases. Our 180° DW model results show that if the cations cannot displace to minimize the A–B cation repulsion, the antiferroelectric phase is more stable than the ferroelectric phase. This suggests that there exists a minimum cation displacement of the ferroelectric phase that is necessary to make it more stable than the antiferroelectric phase. We perform DFT relaxation of the ferroelectric phase of double perovskite oxides and the $\text{PbZr}_{1-x}\text{Ti}_x\text{O}_3$ solid solutions that experimentally are found in antiferroelectric ($\text{PbSc}_{1/2}\text{Ta}_{1/2}\text{O}_3$, $\text{PbIn}_{1/2}\text{Nb}_{1/2}\text{O}_3$, $\text{PbMg}_{1/2}\text{W}_{1/2}\text{O}_3$, and $\text{PbZr}_{1-x}\text{Ti}_x\text{O}_3$, $x < 0.06$) and ferroelectric ($\text{PbSc}_{1/2}\text{Nb}_{1/2}\text{O}_3$, $\text{PbSc}_{1/2}\text{Ta}_{1/2}\text{O}_3$, and $\text{PbZr}_{1-x}\text{Ti}_x\text{O}_3$, $x > 0.06$) phases. We find that the antiferroelectric phase is more stable when the DFT-calculated $D_{B,\text{avg}}$ of the ferroelectric phase is smaller than 0.11 \AA (Figure 7b). Thus, the ferroelectric single-domain B-cation displacement can be used to determine the relative stability of the antiferroelectric and ferroelectric phases, enabling rapid screening of candidate energy storage materials close to the antiferroelectric-to-ferroelectric phase boundary.

The understanding of domain-wall energetics also sheds light on the relative stability of the ferroelectric and paraelectric phases as measured by the Curie temperature T_c . As discussed above, T_c is empirically known to scale as P_0^2 and since 0 K σ_{71} also largely scales with P_0^2 , we obtain that $T_c \sim \sigma_{71}$ at 0 K. The discovered relationship between T_c and σ_{71} is not coincidental but rather is based on the similarity between the local-dipole arrangement at the 71° domain wall and in the disordered high-temperature paraelectric phase that also features misalignment of local dipoles.^[43] The suggested relationship between σ_{71} and T_c is similar to the well-known linear relationship between

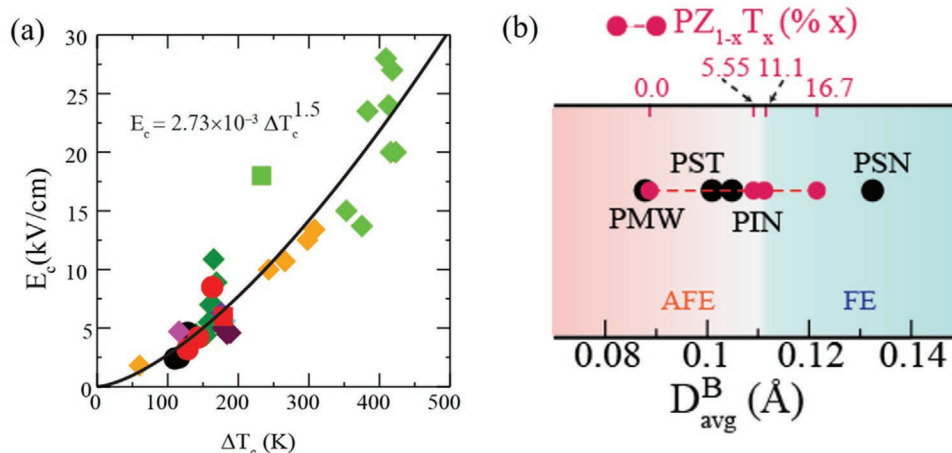


Figure 7. Prediction of antiferroelectric–ferroelectric compositional phase transitions based on FE displacement only. a) Reported experimental coercive field E_c at 300 K vs ΔT_c (K) where $\Delta T_c = (T_c - 300)$ K. T_c is the ferroelectric-to-paraelectric phase transition temperature. The correlation coefficient for the fit is 0.929. References for experimental T_c and E_c data are given in S14 (Supporting Information). b) Phase diagram of the antiferroelectric and ferroelectric phases as a function of the average B-site displacement in the ferroelectric phase obtained from DFT calculations for a series of lead-based double-perovskite and $\text{PbZr}_{1-x}\text{Ti}_x\text{O}_3$ ferroelectrics.

the vacancy-formation energy and the melting temperature in metals. In both cases, the microscopic features of the material at 0 K (σ_{71} and the vacancy-formation energy) measure the energy cost of the configuration that is dominant in the high-energy disordered phase and are therefore correlated with the temperature of the order–disorder phase transition. The relationship between T_c and 0 K σ_{71} is further discussed in a different paper where we show that it can be used to generalize the previously obtained empirical T_c – P_0^2 relationships.^[44]

The above insights into the relative stabilities of antiferroelectric, ferroelectric and paraelectric phases could not have been obtained by considering the ground state 5-atom structure with fixed polarization but are easily revealed through the consideration of the DW defect states with varying polarization. Thus, our dmLGD model shows that the 180°, 90°, and 71° domain walls provide simple model systems for the elucidation of the physics controlling the properties of bulk single-domain ferroelectric perovskite oxide materials.

3. Conclusion

We have studied ferroelectric domain walls using a combination of DFT calculations and analytical modeling using the discrete microscopic LGD (dmLGD) theory. We find that A–B cation repulsion is the interaction that predominantly mediates the coupling of polarization in neighboring unit cells and governs the energy of 180° domain walls. Thus, the energy contribution governed by the gradient term is in fact present even in a single-domain state, and single-domain, 5-atom unit cell calculations can be used to analytically predict domain-wall energies that require much larger (at least 40-atom) DFT calculations. We then demonstrate that the understanding of the different contributions to domain-wall energetics obtained from the simple BaTiO₃, KNbO₃, and PbTiO₃ systems allows the prediction of the potential energy surface for oxygen vacancy migration, and of the polarization switching and dielectric properties controlled by domain-wall movement for ferroelectric materials with a wide range of compositions. Furthermore, the successful use of the domain wall defect to characterize the interactions in the system that are important for the collective behavior of bulk, single-domain materials, along with the previous similar use of the vacancy energy to predict melting points in metals, suggests that the approach of studying the structure and energy of defect states at 0 K for understanding of collective properties at high temperature is general and applicable to wide variety of physical systems.

Supporting Information

Supporting Information is available from the Wiley Online Library or from the author.

Acknowledgements

L.W.M., J.E.S., and I.G. acknowledge the support of the U.S. Army Research Office under Grant W911NF-21-1-0126 and the U.S. Army Research Laboratory under Grant W911NF-19-2-0119. S.P. acknowledges

support from the Army Research Office under Grant W911NF-21-1-0118. I.G. acknowledges support from Israel Science Foundation (Grant No. 1634/18). J.E.S. acknowledges support from the National Science Foundation under Grant CBET 1705440.

Conflict of Interest

The authors declare no conflict of interest.

Author Contributions

A.S. performed DFT calculations and analytical modeling of DWs and AFE. S.Y. developed the E_c – T_c correlation. S.P., Z.G., and L.W. carried out film fabrication and X-ray diffraction measurements. C.J.G.M. performed microwave device fabrication, measurements and analysis. D.C. and L.W. carried out PFM measurements. Z.G. and J.E.S. carried out BST phase diagram LGD modeling. R.A.Y., L.W.M., and J.E.S. supervised the experimental work. I.G. conceived the project and supervised the theory work.

Data Availability Statement

The data that support the findings of this study are available from the corresponding author upon reasonable request.

Keywords

density functional theory (DFT), discrete microscopic Landau–Ginzburg–Devonshire (dmLGD) approach, ferroelectric domain walls, ferroelectric perovskites, order parameters

Received: August 3, 2021

Revised: October 13, 2021

Published online: December 14, 2021

- [1] L. W. Martin, A. M. Rappe, *Nat. Rev. Mater.* **2017**, *2*, 16087.
- [2] J. F. Scott, *Science* **2007**, *315*, 954.
- [3] G. F. Nataf, M. Guennou, J. M. Gregg, D. Meier, J. Hlinka, E. K. H. Salje, J. Kreisel, *Nat. Rev. Phys.* **2020**, *2*, 634.
- [4] P. Sharma, Q. Zhang, D. Sando, C. H. Lei, Y. Liu, J. Li, V. Nagarajan, J. Seidel, *Sci. Adv.* **2017**, *3*, e1700512.
- [5] G. Catalan, J. Seidel, R. Ramesh, J. F. Scott, *Rev. Mod. Phys.* **2012**, *84*, 119.
- [6] A. K. Tagantsev, L. E. Cross, J. Fousek, *Domains in Ferroic Crystals and Thin Films*, Springer, New York **2010**.
- [7] P. Maksymovych, J. Seidel, Y. H. Chu, P. Wu, A. P. Baddorf, L.-Q. Chen, S. V. Kalinin, R. Ramesh, *Nano Lett.* **2011**, *11*, 1906.
- [8] Z. Gu, S. Pandya, A. Samanta, S. Liu, G. Xiao, C. J. G. Meyers, A. R. Damodaran, H. Barak, A. Dasgupta, S. Saremi, A. Polemi, L. Wu, A. A. Podpirka, A. Will-Cole, C. J. Hawley, P. K. Davies, R. A. York, I. Grinberg, L. W. Martin, J. E. Spanier, *Nature* **2018**, *560*, 622.
- [9] S. Liu, R. E. Cohen, *Phys. Rev. B* **2017**, *95*, 94102.
- [10] J. Karthik, A. R. Damodaran, L. W. Martin, *Phys. Rev. Lett.* **2012**, *108*, 167601.
- [11] P. Marton, V. Stepkova, J. Hlinka, *Phase Transitions* **2013**, *86*, 103.
- [12] L.-Q. Chen, *J. Am. Ceram. Soc.* **2008**, *91*, 1835.
- [13] C. T. Nelson, P. Gao, J. R. Jokisaari, C. Heikes, C. Adamo, A. Melville, S.-H. Baek, C. M. Folkman, B. Winchester, Y. Gu, Y. Liu, K. Zhang, E. Wang, J. Li, L.-Q. Chen, C.-B. Eom, D. G. Schlom, X. Pan, *Science* **2011**, *334*, 968.

- [14] D. Lee, R. K. Behera, P. Wu, H. Xu, Y. L. Li, S. B. Sinnott, S. R. Phillpot, L. Q. Chen, V. Gopalan, *Phys. Rev. B* **2009**, *80*, 60102.
- [15] C. Qiu, B. Wang, N. Zhang, S. Zhang, J. Liu, D. Walker, Y. Wang, H. Tian, T. R. Shrout, Z. Xu, L. Q. Chen, F. Li, *Nature* **2020**, *577*, 350.
- [16] B. Meyer, D. Vanderbilt, *Phys. Rev. B* **2002**, *65*, 104111.
- [17] A. Lubk, S. Gemming, N. A. Spaldin, *Phys. Rev. B* **2009**, *80*, 104110.
- [18] W. Ren, Y. Yang, O. Diéguez, J. Íñiguez, N. Choudhury, L. Bellaiche, *Phys. Rev. Lett.* **2013**, *110*, 187601.
- [19] C. Paillard, G. Geneste, L. Bellaiche, B. Dkhil, *J. Phys.: Condens. Matter* **2017**, *29*, 485707.
- [20] P. Marton, T. Shimada, T. Kitamura, C. Elsässer, *Phys. Rev. B* **2011**, *83*, 64110.
- [21] D. Lee, H. Xu, V. Dierolf, V. Gopalan, S. R. Phillpot, *Phys. Rev. B* **2010**, *82*, 14104.
- [22] R. K. Behera, C.-W. Lee, D. Lee, A. N. Morozovska, S. B. Sinnott, A. Asthagiri, V. Gopalan, S. R. Phillpot, *J. Phys.: Condens. Matter* **2011**, *23*, 175902.
- [23] G. Geneste, E. Bousquet, J. Junquera, P. Ghosez, *Appl. Phys. Lett.* **2006**, *88*, 112906.
- [24] M. Taherinejad, D. Vanderbilt, P. Marton, V. Stepkova, J. Hlinka, *Phys. Rev. B* **2012**, *86*, 155138.
- [25] O. Diéguez, P. Aguado-Puente, J. Junquera, J. Íñiguez, *Phys. Rev. B* **2013**, *87*, 24102.
- [26] Y. Wang, C. Nelson, A. Melville, B. Winchester, S. Shang, Z.-K. Liu, D. G. Schlom, X. Pan, L.-Q. Chen, *Phys. Rev. Lett.* **2013**, *110*, 267601.
- [27] A. Chandrasekaran, D. Damjanovic, N. Setter, N. Marzari, *Phys. Rev. B* **2013**, *88*, 214116.
- [28] S. P. Beckman, X. Wang, K. M. Rabe, D. Vanderbilt, *Phys. Rev. B* **2009**, *79*, 144124.
- [29] Z. Jiang, R. Zhang, D. Wang, D. Sichuga, C.-L. Jia, L. Bellaiche, *Phys. Rev. B* **2014**, *89*, 214113.
- [30] B.-K. Lai, I. Ponomareva, I. I. Naumov, I. Kornev, H. Fu, L. Bellaiche, G. J. Salamo, *Phys. Rev. Lett.* **2006**, *96*, 137602.
- [31] S. Boyn, J. Grollier, G. Lecerf, B. Xu, N. Locatelli, S. Fusil, S. Girod, C. Carrétéro, K. Garcia, S. Xavier, J. Tomas, L. Bellaiche, M. Bibes, A. Barthélémy, S. Saïghi, V. Garcia, *Nat. Commun.* **2017**, *8*, 14736.
- [32] R. E. Cohen, *Nature* **1992**, *358*, 136.
- [33] S. Liu, I. Grinberg, A. M. Rappe, *Nature* **2016**, *534*, 360.
- [34] U. Petralanda, M. Kruse, H. Simons, T. Olsen, *Phys. Rev. Lett.* **2021**, *127*, 117601.
- [35] The oxygen vacancies known to stabilize tail-to-tail conducting domain wall can be described by evaluating the changes in a_1 , a_{11} , b_1 due to the presence of the vacancy. It is expected that the vacancy will act as a strong local field that will strongly bias one side of the both A- and B-site double-well potentials. However, the full treatment of this system is outside the scope of this paper.
- [36] L. He, D. Vanderbilt, *Phys. Rev. B* **2003**, *68*, 134103.
- [37] Z. Gu, S. Pandya, A. Samanta, S. Liu, G. Xiao, C. J. G. Meyers, A. R. Damodaran, H. Barak, A. Dasgupta, S. Saremi, A. Polemi, L. Wu, A. A. Podpirka, A. Will-Cole, C. J. Hawley, P. K. Davies, R. A. York, I. Grinberg, L. W. Martin, J. E. Spanier, *Nature* **2018**, *560*, 622.
- [38] I. Grinberg, A. M. Rappe, *Phase Transitions* **2007**, *80*, 351.
- [39] J. C. Wojdef, J. Íñiguez, *Phys. Rev. B* **2014**, *90*, 14105.
- [40] S. Liu, I. Grinberg, A. M. Rappe, *Nature* **2016**, *534*, 360.
- [41] W. J. Merz, *Phys. Rev.* **1954**, *95*, 690.
- [42] S. C. Abrahams, S. K. Kurtz, P. B. Jamieson, *Phys. Rev.* **1968**, *172*, 551.
- [43] A. Bencan, E. Oveisi, S. Hashemizadeh, V. K. Veerapandiyani, T. Hoshina, T. Rojac, M. Deluca, G. Drazic, D. Damjanovic, *Nat. Commun.* **2021**, *12*, 3509.
- [44] S. Yadav, I. Grinberg, *J. Appl. Phys.* **2021**, *129*, 174101.